Structural defects in a Janus MoSSe monolayer: A density functional theory study

Hamid Mehdipour and Peter Kratzer
Faculty of Physics, University of Duisburg-Essen, 47057 Duisburg, Germany

(Received 21 June 2022; revised 12 October 2022; accepted 28 November 2022; published 16 December 2022)

Two-dimensional layered materials with different anions on both faces of each layer, called Janus monolayers, have attracted significant interest due to their unique structural asymmetry perpendicular to the layer, which gives rise to an electric dipole moment that further diversifies the versatile properties of the transition-metal dichalcogenide materials class. However, the synthesis of a material such as MoSSe is prone to the introduction of various point defects, which could significantly modify the electric and optical properties as well as vibrational spectra. Using density functional theory, we provide an in-depth insight into the thermal stability of numerous point-vacancy and antisite defects in the Janus MoSSe monolayer. The structural changes are discussed in terms of the local strain induced by the modified atomic bonding around the defect sites. The electronic structure and linear optical response of Janus MoSSe monolayer with various point defects are studied, and possible fingerprints of electronic transitions due to defects are rationalized. First-principles calculations of phonons are carried out to spot the fingerprint of each point defect in the vibrational spectrum of the Janus MoSSe monolayer. Our systemic study will provide a broad picture of the roles the point defects could play in modifying and tuning the electronic and optical properties of two-dimensional Janus materials and thus help customizing them for certain applications.

DOI: 10.1103/PhysRevB.106.235414

I. INTRODUCTION

Owing to their unique optical and electronic properties, layered inorganic transition-metal dichalcogenide (TMDC) materials have emerged as promising materials that could be used broadly in optoelectronics, sensing, and photocatalytic, as well as many more applications [1–3]. Highly tunable electronic band gap, small dielectric constant, and intrinsic in-plane structural asymmetry play the determining roles in the functioning of such materials in the aforementioned applications. This in-plane symmetry breaking facilitates the exploitation of valley degrees of freedom for optical generation of valley-polarized electrons [4]. Thus, highly accurate spin manipulation could be implemented, paving the way to even more intriguing applications for this class of materials [5]. New interesting electronic properties can be obtained if the out-of-plane inversion symmetry of two-dimensional (2D) TMDC is broken (for example, by applying an electronic field normal to the TMDC plane) [6]. For example, the nonlinear optical response tensor governing, e.g., second harmonic generation, displays additional nonzero elements if the out-of-plane inversion symmetry is broken in these materials [7,8]. In a different context, the electric dipole moment associated with the out-of-plane symmetry breaking promises improved catalytic properties: A monolayer of a single TMDC alone, e.g., a MoS_2 layer, already displays high activity for the hydrogen evolution reaction but just poorly activates the oxygen evolution reaction due to lack of an effective dipole moment which could attract the polar water molecules towards the MoS_2 surface [9]. Thus, MoS_2 and related single-chalcogen compounds can be used only as a photocathode (not as an anode) in a photoelectrochemical cell to drive the reduction of the hydrogen ions into hydrogen molecules. However, structural modification, such as elemental doping, is a promising route to generate a nonzero electric dipole moment [10,11], enabling more effective adsorption of the water molecules.

Janus monolayers, also called multichalcogenide layers, of TMDC materials MXY (M = Mo, W and X, Y = S, Se) are structurally modified TMDCs that have attracted enormous interest recently due to their extra intrinsic electrical and optical properties compared to the parent TMDC materials of MX_2 [7,8,12,13]. This is because, in this type of TMDC material, the out-of-plane structural symmetry is broken as a result of two different chalcogen atoms sitting at mirror-symmetric lattice sites surrounding transition-metal atoms. The out-of-plane asymmetry gives rise to the emergence of a tangible electric dipole moment from which a net electric field, directed from Se atom to S atom normal to the layer, is generated [11]. The normal electric field polarizes the electronic system [7], causing strong Rashba spin-orbit coupling, which then enhances spin Hall conductivity in valence bands [14]. The broken-symmetry-induced electric field also enhances the nonlinear optical response of layers [8]. The strength of electric charge polarization is very sensitive to the stoichiometry of MXY monolayers and their possible stacking (up to the bulk counterpart of monolayers). This area of research on the Janus materials has been explored extensively using real-time, first-principles methods that compute the electronic structure and nonlinear susceptibility of Janus monolayers of TMDCs with different stoichiometries of the chalcogens [15] and different stacking patterns [8,12].

While Janus materials are attractive for numerous reasons, as outlined above, their availability and structural integrity still pose a challenge to materials scientists. Although nearly a decade ago, the TMDC structure with two different chalcogenide atomic surfaces was theoretically proven to be stable and to have new intrinsic electronic properties [16], experimental work was limited to the synthesis of a MX_2 structure with only some level of chalcogenide impurities substituting the "parent" chalcogen X. Recently, development in experimental equipment and techniques has brought about the opportunity to fabricate Janus monolayers with two different uniform chalcogenide layers enclosing a transition-metallic layer [12,17,18]. Like other 2D materials [19], the formation of defects during the synthesis process is very likely unavoidable because of the high-temperature condition imposed in the multistep synthesis process of Janus MoSSe [7,20]. Several types of structural defects, such as point vacancies and antisite defects, grain boundaries, etc., could emerge over the course of the synthesis or exfoliation process [21,22]. Depending on the process taken, the prevailing type of defect or its distribution may change.

Numerous experimental works have been carried out to investigate the aforementioned and some other new intriguing properties of pristine Janus 2D materials [6,7,12,15,23]. Recently, theoretical works based on first-principles methods have been carried out to explain the emergence of important properties for the pristine Janus materials [8,15,24]. Also, theoretical studies suggested that magnetism can be induced by the point defects in Janus layers and by imposing an external strain, and the magnetism characteristics may well be modulated by varying the tensile strain [6]. The nonzero magnetic moment of the sulfur vacancy proposed in this work seems debatable; it would require that two electrons, one in each of the dangling bonds introduced by the S vacancy, align their spins to form a spin triplet. So far, there has been no experimental measurement that could address such prediction.

Apart from this open question, the formation of defects in Janus layers is a topic in its own right and deserves further studies. The formation of any structural imperfection significantly alters the electronic, optical, and mechanical characteristics of these ultrathin materials. If a spin-polarized state of an isolated defect is thermodynamically more favorable, one could envisage incorporating such defective materials into spintronics devices, possibly for spin-based information storage and computing [25]. An isolated point defect could provide a suitable two-level system for a single-photon emitter. A negatively charged isolated point-vacancy and antisite defect could provide some dispersionless midgap states, and polarized light can be used to control its excited state. A structural defect with these characteristics, if thermodynamically stable, would thus be a promising candidate for a single-photon emitter [26].

Also, in the field of surface chemistry and catalysis, defects may play an important role. A sufficiently high concentration of a defect of a specific type could enormously alter the chemistry of the surface as well as the total nonzero electric dipole moment (electric field) of a Janus MoSSe layer, thus providing suitable sites for the adsorption of molecular species and for accelerating this process. Also, the intrinsic electric field in MoSSe can enhance the dielectric screening, thus reducing the exciton binding energy. The more loose binding between photogenerated excited electrons and holes largely decelerates their recombination. Under this condition, the electrons and holes can live longer and are more likely to participate in water molecule oxidation and hydrogen-ion reduction, respectively [27]. Therefore, understanding how the intrinsic electric dipole moment of a MoSSe single layer may be changed due to defect formation is of interest to designing suitable catalyst layered materials.

In this work, we study the thermal stability of the most likely point defects that can form during the multiple-step synthesis of 2H-MoSSe. The changes in the electronic structure upon the introduction of defects into the MoSSe structure are investigated and discussed in detail, and the possibility of formation of a localized nonzero magnetic moment (at the defect sites) is fully examined *at varying concentrations*. The dipole moment of MoSSe is quantified, and its variation upon structural change (due to the point defects) is rationalized. Furthermore, the fingerprint each defect may have in the phonon mode spectrum of the Janus MoSSe ML is studied, and the origins of such new features are brought into the light.

II. COMPUTATIONAL METHODOLOGY

A. Density functional theory of defects in Janus MoSSe monolayer

We study the thermal stability of possible defects in the monolayer of Janus MoSSe materials and their electronic structure and linear-optical responses using a periodic density functional theory (DFT) model of Janus 2H-MoSSe single layer with a single structural defect. The relaxation and postprocessing electronic structure calculations were carried out using the periodic-DFT model implemented in the FHI-AIMS code [28]. The optical properties were calculated using random-phase approximation. The FHI-AIMS code provides an all-electron description in which each single-particle Kohn-Sham (KS) electronic orbital is expanded as a linear combination of numeric atom-centered basis functions.

Figure 1 displays possible point-vacancy and antisite defects in a large (4×4) supercell of MoSSe (with cross-section area 12.91×12.91 Å^2) constituted by 48 atoms of transition-metal Mo, S, and Se atoms. Isolated vacancy defects are formed by removing one atom or a pair of atoms from the MoSSe single layer. The substitution of one type of atom with another forms the antisite defects. To treat exchange-correlation interactions of electrons, generalized-gradient approximation (GGA) parametrized as PBE [29] is used. The Broyden-Fletcher-Goldfarb-Shanno method [30] was used to relax atomic positions along the potential energy surface, and the maximum residual force component per atom was set at 5.0×10^{-3} eV/Å, while a k mesh of $6 \times 6 \times 1$ was used to compute the Hellmann-Feynman forces exerted on each atom. To obtain converged total energy and carry out the electronic structure and optical calculations, a Monkhorst-Pack [31] k mesh of $17 \times 17 \times 1$ was used to sample the k points for integration over the first Brillouin zone. A vacuum space of nearly 20 Å is added in the perpendicular direction to avoid the artificial interactions between the monolayer and its image replica perpendicular to the monolayer. Also,

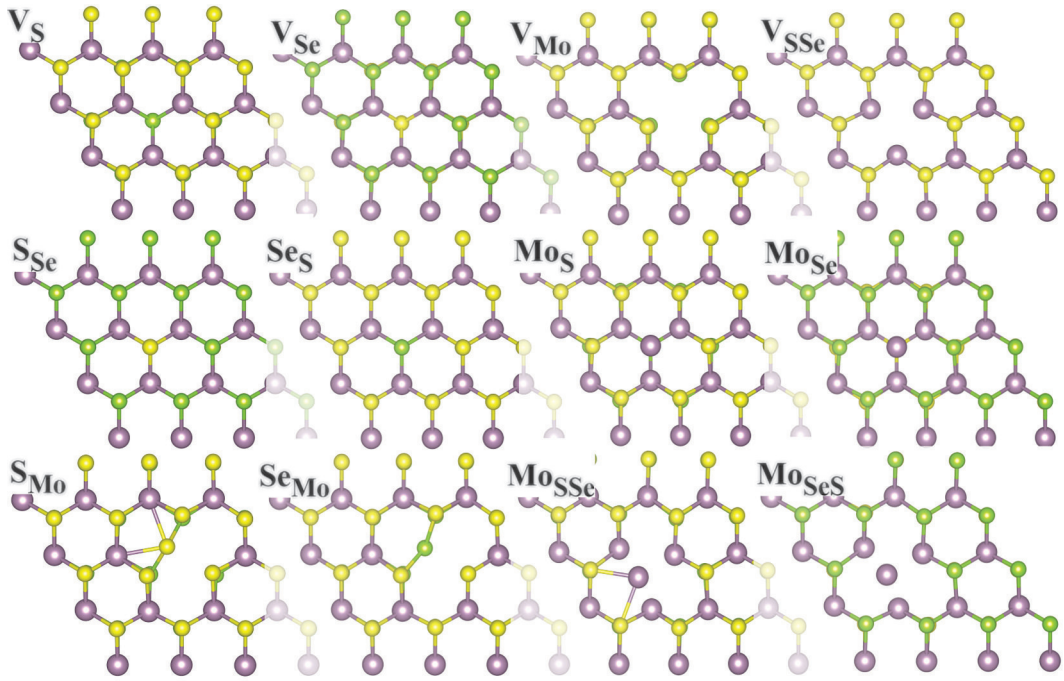

FIG. 1. Relaxed geometries of MoSSe ML containing point-vacancy and antisite defects. Se, Mo, and S atoms are represented by green, violet, and yellow balls.

spin-polarization (spin-unrestricted) calculations were carried out to explore thermodynamically stable triplet ground states of all defect geometries, and comparisons are made against previous reports in the literature. The so-called "tight" basis set is employed to carry out the relaxation of atomic positions. To obtain more accurate energy band structures of relaxed MoSSe geometries, we take into account the spin-orbit coupling (SOC) by performing second-variational SOC calculations. In the FHI-AIMS code, the SOC calculation is performed as a postprocessing step with $2N$ KS states obtained in the last self-consistent field calculation [32], and a "really tight" basis set is used for expansion of the KS single-electron functions [28]. The really tight basis for a chemical element has a larger maximum angular momentum number for expansion of charge density difference and uses a denser angular grid point per radial integration shell [28].

To examine the relative stability of the defective structures studied in this work, we calculated the formation energies of the structures using

$$E_{\mathrm{f}} = E_{\mathrm{tot}} - E_{\mathrm{pristine}} - \sum_i \Delta N_i \mu_i,$$

where E_{tot} and E_{pristine} are total energies of the MoSSe supercell with and without defects, respectively. μ_i is the chemical potential of defect element i, and ΔN_i is the variation of atomic number during the introduction of defect, $\Delta N < 0$ when the element is removed, and $\Delta N > 0$ otherwise. If one element replaces another element, that one atom is substituted by another atom of a different type, the chemical potential of the missing atom is added, and that of the substitutional element is subtracted from the above equation. Here we choose bulk Mo as the elemental system reference to determine the chemical potentials. The chemical potentials of S and Se are determined from the relation

$$\mu_{\mathrm{Mo}} + 2\mu_{\mathrm{S}} = E_{\mathrm{MoS_2}}, \quad \mu_{\mathrm{Mo}} + 2\mu_{\mathrm{Se}} = E_{\mathrm{MoSe_2}},$$

where $E_{\mathrm{MoSe_2}}$ and $E_{\mathrm{MoSe_2}}$ are the formation energies of these TMDCs from elemental bulk phases. These equations also limit the accessible range of μ_{Mo} in equilibrium. For example, the upper boundary of $\mu_{\mathrm{Mo}}^{\mathrm{max}}$, corresponding to Mo-rich condition is given by energy per atom of hexagonal lattice of bulk Mo, and the lower μ_{Mo} boundary corresponding to S- or Se-rich conditions is defined as $\mu_{\mathrm{Mo}}^{\mathrm{min}} = E_{\mathrm{MoX_2}} - 2\mu_X^{\mathrm{max}}$, where X = S or Se, and μ_X^{max} is computed for the primitive unit cell of bulk X.

In bulk semiconductor physics, the concept of the charge state of a defect turned out to be very useful. The defect formation energy in its various charge states is plotted as a function of the chemical potential of the electrons (the "Fermi level," as it is often called), a quantity that is set by the concentration of other defects or dopants in the material. The concept of a spatially (nearly) homogeneous chemical potential relies on the fact that any charge on a defect is dielectrically screened by the three-dimensional (3D) bulk, such that different defects interact only via defining the position of the chemical potential of the electrons. In a 2D material, dielectric screening is strongly reduced. As a result, charged defects in the material or in the substrate influence each other directly via their electric fields. Moreover, the efficiency of screening, and thus also the electrostatic energy and hence the formation energy of a charged defect, depend on the nature of the substrate and the material covering the 2D layer. In order to avoid such complications, we consider in the following all defects in their neutral state only. Previous works, using techniques from bulk semiconductor physics modified appropriately for 2D materials [19,33], have studied charged defects in MoS_2. They concluded [19] that most point defects

TABLE I. Formation energies under Mo-rich condition (E_f), electronic band gap (E_g), total magnetic moment (M_{tot}), and total electric dipole moment per surface area (D_{tot}) of relaxed geometries of pure MoS_2, $MoSe_2$, and MoSSe monolayers with possible point-vacancy and antisite defects. Also, the tensile strain [$\Delta l/l(\%)$)] (with respect to the pristine MoSSe monolayer) imposed on the atomic bonds surrounding the defect site are given.

	E_f (eV)		E_g (eV)		D_{tot} (10^{-2} e/Å)		$M_{tot}(\mu_B)$	$\Delta l/l(\%)$
	PBE	HSE	PBE	HSE	PBE	HSE		
MoS_2			1.70	2.17	0.00	0.00		
$MoSe_2$			1.44	1.84	0.00	0.00		
MoSSe			1.55	2.01	3.42	3.57	0	
V_S	2.06	2.34	0.99	1.49	3.40	3.58	0	−2.21
V_{Se}	1.80	2.07	0.99	1.54	3.24	3.37	0	−4.20
V_{Mo}	5.44	6.68	0.22	0.61	3.10	3.26	0	+2.70
V_{SSe}	3.74	4.28	0.92	1.46	3.28	3.44	0	−11.00
S_{Se}	−0.05	−0.31	1.54	2.09	3.25	3.37	0	−1.00
Se_S	−0.06	−0.26	1.55	2.07	3.15	3.26	0	+1.00
Mo_S	5.40	4.96	0.28	1.28	1.56	1.48	2	−3.00
Mo_{Se}	5.16	4.87	0.21	1.25	4.45	4.78	2	−3.90
S_{Mo}	5.57	6.63	0.45	0.81	2.85	2.95	0	
Se_{Mo}	5.54	6.38	0.00	0.66	2.88	2.99	2	
Mo_{SSe}	6.73	6.86	0.66	1.17	1.52	1.42	0	−6.57,+9.08
Mo_{SeS}	6.97	7.15	0.54	1.04	4.38	4.71	0	−4.18,+11.09

are stable in their neutral state, with the exception of the V_S and S_{Mo} defects that occur in a singly negative charge state for the Fermi energy getting close to the conduction band edge. We expect similar phenomena for MoSSe, although the band gap is somewhat smaller for MoSSe compared to MoS_2 which makes the formation of charged states less likely.

Following the evaluation of the stability of the relaxed defect geometries, we calculate the electronic band structure as well as atom-projected and angular-momentum-projected densities of states for each geometry. The defect-induced energy bands and orbital contributions to the defect energy levels are displayed and discussed. Since the Janus MoSSe monolayer is a polar material (due to the different electronegativity of the chalcogen atoms), we include a dipole correction, i.e., an adjustable dipole layer in the middle of the vacuum space is applied to nullify any electric fields in the vacuum. This allows us to avoid the artificial dipole interaction between the ML and its replica normal to the ML plane. Simultaneously, the potential jump calculated in the vacuum region above the polar MoSSe ML is used to estimate the electric dipole moment density of the ML MoSSe [34]. Moreover, the electric dipole moment density D_{tot} of each geometry is computed, and the effect of structural changes (due to defects) on the magnitude of the electric dipole moment density is investigated.

Range-separated hybrid potentials, such as HSE06, approximate the band gaps of the semiconductors and the positions of midgap defect states more accurately. This is because the hybrid potentials give a better description of valence states (through partial inclusion of nonlocal Hartree-Fock exchange term) and partly correct the self-interaction error as well [35]. Given the same lattice constants obtained for MoSSe monolayer using semilocal PBE and hybrid HSE06 functionals, we carried out single-point energy calculation using the hybrid functional. The band gaps calculated using the HSE06 functional are presented in Table I.

B. Random phase approximation of linear optical response of defects

Studying the optical characteristics of the MoSSe would help us get complementary insight into the electronic structures of the material system and the role of defects introduced into its structure, thus suggesting possible effects they could have on its overall performance in the envisaged applications. In this work, the frequency-dependent dielectric tensor $\epsilon_{ij}(\omega)$ is calculated using the independent-particle random-phase approximation (RPA), based on energy eigenvalues and Kohn-Sham orbitals obtained in the ground-state self-consistent field (SCF) calculation of the relaxed geometries. In the RPA formalism, the momentum matrix elements are taken into account for both interband and intraband transitions. However, since the single-particle quantities contribute to quantifying the dielectric tensor, many-body effects such as excitonic effects are not included. The frequency-dependent dielectric tensor $\epsilon_{ij}(\omega)$ is calculated using the Kubo-Greenwood formula

$$\epsilon_{ij}(\omega) = \delta_{i,j} - \frac{4\pi}{V_{\text{cell}}\omega^2}\sum_{n,\mathbf{k}}\left(-\frac{\partial f_0}{\partial \epsilon}\right)_{\epsilon_{n,\mathbf{k}}} p_{i;n,n,\mathbf{k}}\, p_{j;n,n,\mathbf{k}} + \frac{4\pi}{V_{\text{cell}}}\sum_{\mathbf{k}}\sum_{c,v}\frac{p_{i;c,v,\mathbf{k}}\, p_{j;c,v,\mathbf{k}}}{(\epsilon_{c,\mathbf{k}} - \epsilon_{v,\mathbf{k}} - \omega)(\epsilon_{c,\mathbf{k}} - \epsilon_{v,\mathbf{k}})^2},$$

where $\epsilon_{v,\mathbf{k}}$ and $\epsilon_{c,\mathbf{k}}$ denote the occupied valence and unoccupied conduction energy levels, respectively. f_0 is the Fermi-Dirac occupation function, $p_{j;c,v,\mathbf{k}}$ are the momentum matrix elements, and V_{cell} is the supercell volume.

As mentioned earlier, a "really tight" basis is used to have a more accurate estimation of the higher-lying energy levels so that a more complete and accurate description of the transition matrix elements is taken into account in the RPA method. Following the calculation of the imaginary part of the dielectric tensor, the absorption coefficients of MoSSe geometries are

obtained, and some comparison with available experimental measurements is carried out.

C. Phonon-vibrational spectrum and thermal properties of defects

The finite-displacement method as implemented in PHONOPY code [36] is used to calculate the vibrational frequencies and corresponding density of states (DOS). A supercell of (2×2) of the supercell (4×4) is constructed, and 286 displaced geometries are generated. Given the very large number of generated displaced geometries, forces are computed with a less-dense Monkhorst-Pack k mesh of $3 \times 3 \times 1$. Then the force constants for each geometry are calculated and collected. Following these steps, the phonon density of states $[g(\omega)]$ for each geometry is calculated at a converged q mesh of $40 \times 40 \times 1$. For further analysis, the average phonon frequency

$$\bar{\omega}_{\text{ave}} = \frac{\int_0^{\omega_{\max}} \omega g(\omega) d\omega}{\int_0^{\omega_{\max}} g(\omega) d\omega}$$

is calculated for all vacancies and antisite defects.

III. RESULTS AND DISCUSSION

A. Point defects in Janus MoSSe monolayer: Thermal stability

Optimizing the MoSSe monolayer (ML) lattice constant at different levels of theory (treating electron-electron exchange-correlation interactions), PBE [37], LDA [38], and HSE06 [39], suggests that the local-density approximation (LDA) underestimates the lattice constant (3.16 Å), whereas the generalized-gradient approximation (PBE), as well as the hybrid functional (HSE06), give the lattice constant of 3.23 Å which is close to the experimentally measured one [7]. Using the same PBE functional, the lattice constants of 3.16 and 3.29 Å are calculated for MoS_2 and $MoSe_2$, respectively. The corresponding experimental values are 3.15 [40] and 3.3 Å [41], respectively.

Here, we focus on the 2H type of the Janus MoSSe monolayer since, like for the bulk MoSSe, it is thermally more stable by 440 meV than the $1T'$ phase. Only by doping electrons above a certain concentration into the 2H-MoSSe thus destabilizing the 2H structures, the transformation into the $1T'$ phase is possible [42].

1. Formation enthalpies

The enthalpy of formation ΔH_{f} of Janus MoSSe ML out of MoS_2 and $MoSe_2$ is +54 meV (12 meV) using the PBE (HSE06) functional. This indicates that under the standard thermal condition, i.e., at room temperature, the formation of MoSSe is not thermally favorable. Thus, merely under nonequilibrium conditions or by implementing sophisticated multiple-step synthesis approaches, synthesizing this class of materials is feasible [7,20].

The relative stability of point defects under thermal equilibrium can be evaluated by calculating the formation energy as the primary indicator of more stability of one defect over another. Table I shows the formation energies obtained for all the relaxed geometries of Janus MoSSe MLs without and with point defects studied in this work. We note that formation energies calculated with the HSE06 functional are about 10% to 20% larger than those obtained with PBE in most cases. Among the point-vacancy and antisite defects explored for Janus MoSSe monolayer, the antisite defects S_{Se} and Se_S have the lowest formation energies. Also, it is seen that Janus MoSSe containing the S_{Se} antisite defect is thermally more stable than the parent pure MoSSe structure. This can be related to the above observation that ΔH_{f} for forming MoSSe from MoS_2 and $MoSe_2$ is positive, and hence MoSSe has a tendency to disproportionation. Moreover, the tensile strain for such S_{Se} and Se_S defects are the smallest, which goes in line with the low formation energies (the least destabilization of the monolayer structure) calculated for such antisite defects. Our calculations show that, among the MoSSe MLs with vacancy defects, V_{Se} and V_S are the most stable geometries. The formation energy of V_S is larger than that of V_{Se}, possibly because the S atom has a greater electronegativity than the Se atom. This makes the removal of an S atom from the ML energetically more expensive. This finding is in good agreement with the previous theoretical works [6,43].

To relate our findings to the experiment, we use experimental data on defects on MoS_2 since data about defects in MoSSe are not yet available. Experimental observation based on atomic-resolved electron microscopy (STEM) suggests that S vacancies are the most abundant point defects formed during the production of MoS_2 monolayers using nonthermal methods, such as mechanical exfoliation, at room temperature [21,22]. Qualitatively speaking, since the vapor pressure of sulfur is higher than that of Mo, a stronger deficiency of S atoms than Mo atoms is expected after exfoliation when the equilibrium of both these elements with a gas phase is established. In the language used here, this means that exfoliation conditions tend to be Mo rich, with relatively lower formation energies of V_S and V_{Se}.

Given the larger ionic radius of Mo atoms, replacing either the S or Se atom with the Mo atom could give rise to a notable distortion in the structure of 2H-MoSSe. This is because such replacement brings the antisite (guest) Mo atom and Mo atoms into a closer distance (see Table I) and, also, the distances between Mo atoms surrounding the defect site become shorter.

As our data suggest, the formation energy for such antisite defects is larger (nearly 2.5 eV) than for point-vacancy defects. Thus, one can conclude that the formation of such antisite defects in the MoSSe ML is less likely to occur. However, as pointed out earlier, under high-temperature growth conditions, typically required in physical vapor deposition and other similar methods, antisite point defect Mo_S/Mo_{Se} becomes more frequent and even the dominant intrinsic defect. This can be rationalized by looking at the stages of the growth process: First, elemental precursors are sublimated from a source and transported by a carrier gas to the substrate where the TMDC monolayer is formed. Due to the higher vapor pressure of S (Se) under gas-solid equilibrium, fewer S (Se) atoms tend to contribute to condensation (forming a TMDC molecular unit on the substrate). As a result, there will be an excess concentration of Mo atoms, which then leads to some S sites being filled by extra Mo atoms when the TMDC molecular units are formed [22,44]. The same scenario is expected in forming Mo_{SSe} or Mo_{SeS} defects due

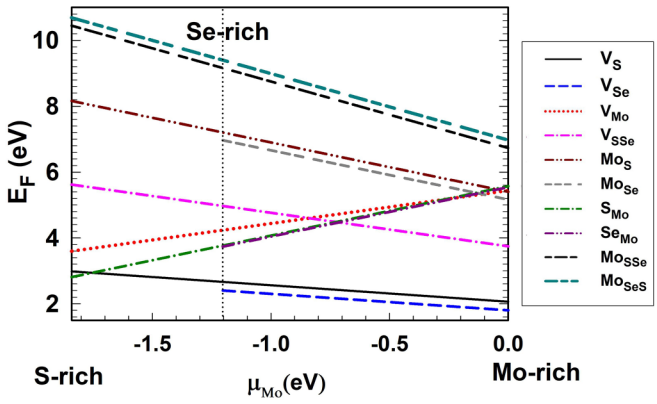

FIG. 2. Formation energies of Janus MoSSe ML with the point-vacancy and antisite defects as function of the chemical potential of Mo with Mo-rich condition (on the right) and S- and Se-rich conditions (on the left) calculated with the PBE functional.

to a severe lack of S atoms when forming MoSSe molecular units in thermal synthesis methods.

To obtain a clear view of the formation energy change with the chemical potential, Fig. 2 displays the formation energies of the point-vacancy and antisite defects as functions of the chemical potential of Mo. Because the Janus MoSSe contains two different chalcogen atoms, two limits, S- and Se-rich conditions, against the Mo-rich limit, can be defined. One can see that V_{Se} is more stable than V_S for the entire range of μ_{Mo} (Fig. 2). The same trend is clearly observed when the two chalcogen atoms are replaced by the more bulky Mo atom (see Fig. 2). As expected, the Se/S vacancy is formed under the Mo-rich condition, and vice versa. Also, one can see that under the extreme Mo-rich condition, the Mo vacancy is slightly more stable than the antisite defects S_{Mo} and Se_{Mo}, i.e., when one Mo atom is replaced by one chalcogen atom.

2. *Magnetic moments*

To explore the possibility of the formation of a nonzero magnetic moment localized in the defect region, we carried out the relaxation of atomic positions under the fixed magnetic moment of $2\,\mu_B$ ($S = 1$, a triplet state) (see Table I). It is seen that among the vacancies and antisite defects studied, only Mo_{Se} and Se_{Mo} could carry nonzero magnetic moments. This is because the total-energy differences between zero- and $2\,\mu_B$-magnetic-moment states of these defect geometries fall in the range 50–230 meV, which means the formation of defect regions with a nonzero magnetic moment is thermodynamically more favorable than the regions with a zero-magnetic moment in the MoSSe ML structure. Also, it should be noted that the energy difference is as small as 2 meV for the Mo_S defect. This indicates that the formations of antisite-defect regions with zero and nonzero magnetic moments are equally likely at growth temperature when one Mo atom substitutes one S atom during the synthesis of the Janus MoSSe ML.

Here we have shown that the emergence of the defect-induced nonzero magnetic moment strongly depends on the type of defect introduced into the MoSSe structure. If a magnetic moment exists due to the presence of a specific defect, its magnitude depends on the concentration of the defect [45]. In 2D Janus MoSSe, the local nonzero magnetic moment, caused by presence of antisite defects Mo_S, Mo_{Se}, and Se_{Mo}, may vanish at a higher defect concentration. Moreover, the magnetic response of Janus MoSSe with antisite defects Mo_S, Mo_{Se} vanishes when the number of defects in a (4×4) supercell is increased by one (the defect concentration increasing from 6.2% to 12.5%) [46].

Upon the formation of a single Mo_S defect, three Mo nonbonding orbitals (dangling bonds) exist, out of which two are occupied, each with an unpaired electron with the same spin. With more antisite defects present, the nonbonding half-filled orbitals interact and form fully bonding orbitals. Thus, clustering of antisite defects favors a singlet configuration. In contrast, the Janus MoSSe with antisite defect Se_{Mo} still carries a nonzero magnetic moment even at a higher defect concentration. This can be explained by observing that the Se atom relaxes away from the Mo site (see Fig. 1). Upon the formation of one Se_{Mo} defect, two dangling bonds are formed at the nearby chalcogen atoms (one bond per atom). Substituting more center-layer Mo by Se atoms, more dangling bonds are formed, breaking the bond and pushing the Se atoms out of the MoSSe plane. Thus, the half-filled orbitals remain. As a result, the localized nonzero magnetic moment due to the defect is preserved.

Contrary to previous reports on nonzero magnetic moment associated with V_S [6], our study suggests that point S and Se vacancy defects (V_S and V_{Se}) carry no localized magnetic moment. The converged total energies of the relaxed geometries of V_S and V_{Se} obtained under a fixed nonzero magnetic moment (of $2\,\mu_B$) are higher than the total energy of the zero magnetic moment. Performing a similar set of calculations using a hybrid functional, like HSE06, supports such a conclusion [46].

To put this in more context, when an S atom is removed (from the pure Janus MoSSe), the Mo dangling bond states at the now under-coordinated Mo atoms (surrounding the S vacancy) form a state space consisting of nonbonding $4d$ orbitals that are either fully occupied by two electrons or completely unoccupied. Under this circumstance, a singlet-state electronic configuration is favored. In addition, we note that previous theoretical and experimental works concluded that room-temperature ferromagnetic response from the MoS_2 can be measured only when a localized $1T'$ structural phase can be incorporated into 2H-MoS_2 ML structure with S vacancy [47]. Likewise, exerting high-enough tensile strain on the MoS_2 structure also could induce the magnetic moment at the vacancy site due to the breaking of metallic Mo-Mo bonds surrounding the defect site. The bond breaking gives rise to the formation of nonbonding Mo $4d$ orbitals filled by parallel-spin electrons, which amounts to a magnetic moment of $2\,\mu_B$ [48]. Thus, the formation of a triplet state is favored only under high tensile strain.

3. *Local strain*

Structural changes occur when point vacancies are introduced into the MoSSe ML structure. They are evaluated by measuring the interatomic distances (l) between the three atoms surrounding the point-defect site. In most cases, all

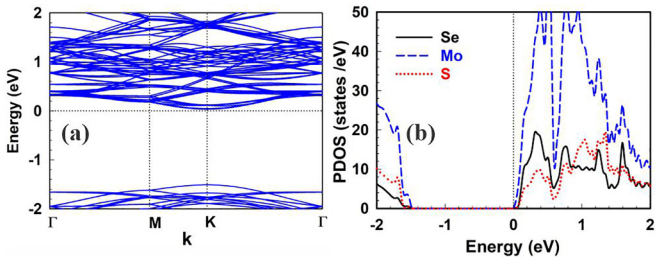

FIG. 3. Electronic band structures (a) and the atom-projected densities of states (b) of Janus MoSSe modeled using a (4×4) supercell.

three distances for each geometry are measured to be the same, forming an equilateral triangle enclosing the defect site. One can see that removing one chalcogen atom, either S or Se, brings the Mo atoms (surrounding the defect site) closer together (see Fig. 1). This contraction is more significant for V_{Se} than for V_S. This can be rationalized by looking at the amount of positive partial charge induced on the neighboring Mo atoms [46]. The larger Mo positive charges indicate a more compact electron cloud around Mo, which in turn leads to a smaller distance between the Mo atoms surrounding the defect. The contraction of the interatomic distance is larger when both chalcogen atoms from the same atomic column are removed from the 2H-MoSSe structure (V_{SSe}). The contraction reaches up to an 11 %, which is consistent with the larger contraction (in forming V_{2S}) measured for MoS_2 [49]. Also, the same analogy can be used to explain the level of exerted local strain between other pairs of the antisite defects (S_{Se} and Se_S, and Mo_S, and Mo_{Se}) [46].

B. Electronic structure of pure Janus MoSSe monolayer and defect geometries

To characterize the electronic structure of point defects, we use information from different sources: The dipole moment of the MoSSe perpendicular to the film plane tells us about the charge distribution of the constituent atoms and how it changes due to the defects. The electronic band structure calculated in a (4×4) supercell shows defect-related levels or defect-induced bands. Atom-projected angular-momentum-projected densities of states (PDOS) can reveal the role of constituting chemical elements and their angular-momentum orbitals in forming the band edges, namely, the valance band maximum (VBM) and conduction band minimum (CBM).

1. Pure MoSeS

Figure 3 displays atom-projected densities of states for Janus MoSSe without defects. Calculation of atom-projected and angular-momentum-resolved densities of states suggests that the band edges states (CBM and VBM) are constituted mainly by the 4*d* orbitals of Mo atoms (see Fig. 3, plus additional information in the Supplemental Material (SM) [46]. Also, the 4*p* orbitals of Se atoms largely contribute to the CBM states.

In pure 2H-MoSSe, the *d* orbitals of Mo hybridize, and the molecular orbitals transform according to the one-dimensional A_1 and the two-dimensional E representation of the symmetry group C_{3v}. For the geometry we have chosen, the vector of the intrinsic electric dipole moment of single-layer MoSSe points in the $+z$ direction. This is because the S atom is more electronegative than the Se atom, and the Se and Se atoms reside at the top (= positive z) and bottom (= negative z) sides of the Mo atomic layer, respectively. Defect formation may lead to an increase or decrease relative to this intrinsic value (see Table I). Figure 3(a) shows the electronic band structure of supercell (4×4) of pure MoSSe over a specific k path of high-symmetry points of the first Brillouin zone (FBZ). Since the supercell (4×4) is used to model MoSSe ML, the conduction band minimum and valance band maximums are located at the same high-symmetry point K of FBZ. Thus, there exists a direct band gap for Janus MoSSe ML, and it is estimated at 1.55 eV with the PBE functional (2.01 eV with the HSE06 functional).

Including spin-orbit interaction removes the degeneracy of energy levels, giving rise to energy-level splitting, which is more pronounced for heavy transition metals with *d* orbitals [50]. For a better assessment of the effect of spin-orbit interaction on the band structure, plots zooming in on the valence and conduction band edges are presented in the SM [46]. The energy-level splitting in the bottom-most conduction bands amounts to 14 meV, while the splitting could reach up to over 30 meV in the valence bands.

2. Anion vacancies

From the calculated formation energies, one can find that the anion vacancies V_S and V_{Se} are the thermodynamically most likely defects that are associated with deep levels in the band gap. Removing an anion creates three dangling bonds at three adjacent Mo atoms and reduces the count of valence electrons by two. Consequently, only one of the dangling orbitals leads to an occupied defect state. As seen from Figs. 4(a) and 4(b), this state is located directly above the VBM for V_S, while it cuts below the VBM for V_{Se}. In addition, there are two (almost degenerate) unoccupied defect levels. As seen from the PDOS in Fig. 5(a), these states have predominantly Mo character. Interestingly, the gap between the valence band minimum and these defect states is functional dependent (0.99 eV in PBE, ∼1.5 eV in HSE06) which confirms that these are "deep" levels that do *not* move with the valence band edge. Additional information about the splitting of these states under the influence of SOC is provided in the SM [46].

3. Mo vacancy

Removing a Mo atom from the central layer of the MoSSe film creates six dangling bonds. Consequently, large parts of the band gap are filled with defect states, leaving a gap of 0.22 eV in PBE (0.61 eV in HSE06) in the presence of V_{Mo}. As expected, the occupied and unoccupied defect-induced bands have a strong contribution from chalcogen orbitals, while the Mo orbital contribution is larger in unoccupied than in occupied orbitals [see Fig. 5(c)]. Therefore, one could expect that the SOC effect, which is most significant for *d* orbitals of heavy elements, becomes notable for the unoccupied orbitals. The SM [46] provides support for such a conclusion, and it is seen that the unoccupied defect states undergo

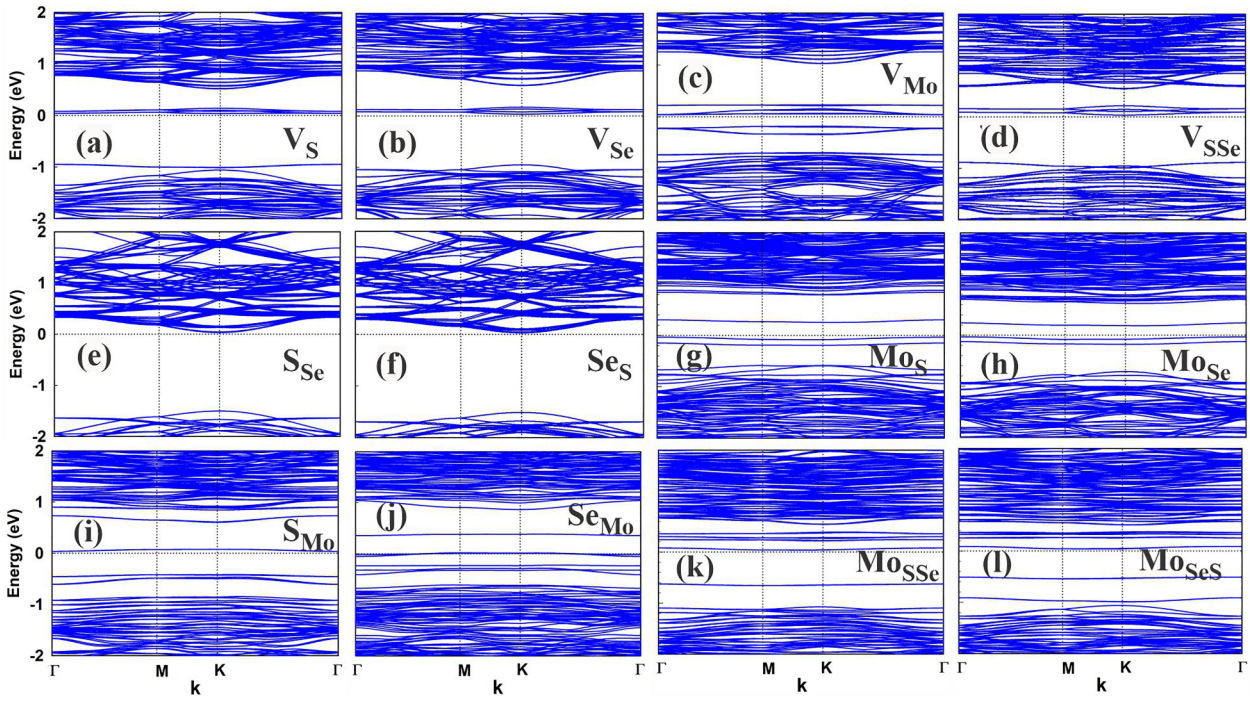

FIG. 4. Electronic band structures of Janus MoSSe with point-vacancy and antisite defects.

approximately 10 meV larger band splitting (especially at the high-symmetry point K).

The total electric dipole moment is reduced by V_{Mo}, indicating that the polarization of the Mo charge density contributes significantly to the overall dipole moment, and hence the intrinsic dipole of the MoSSe layer gets diminished if one Mo atom is missing.

The double vacancy V_{SSe}, where two anions are missing directly above each other on different sides of the MoSeS film, displays an electronic structure that is essentially a

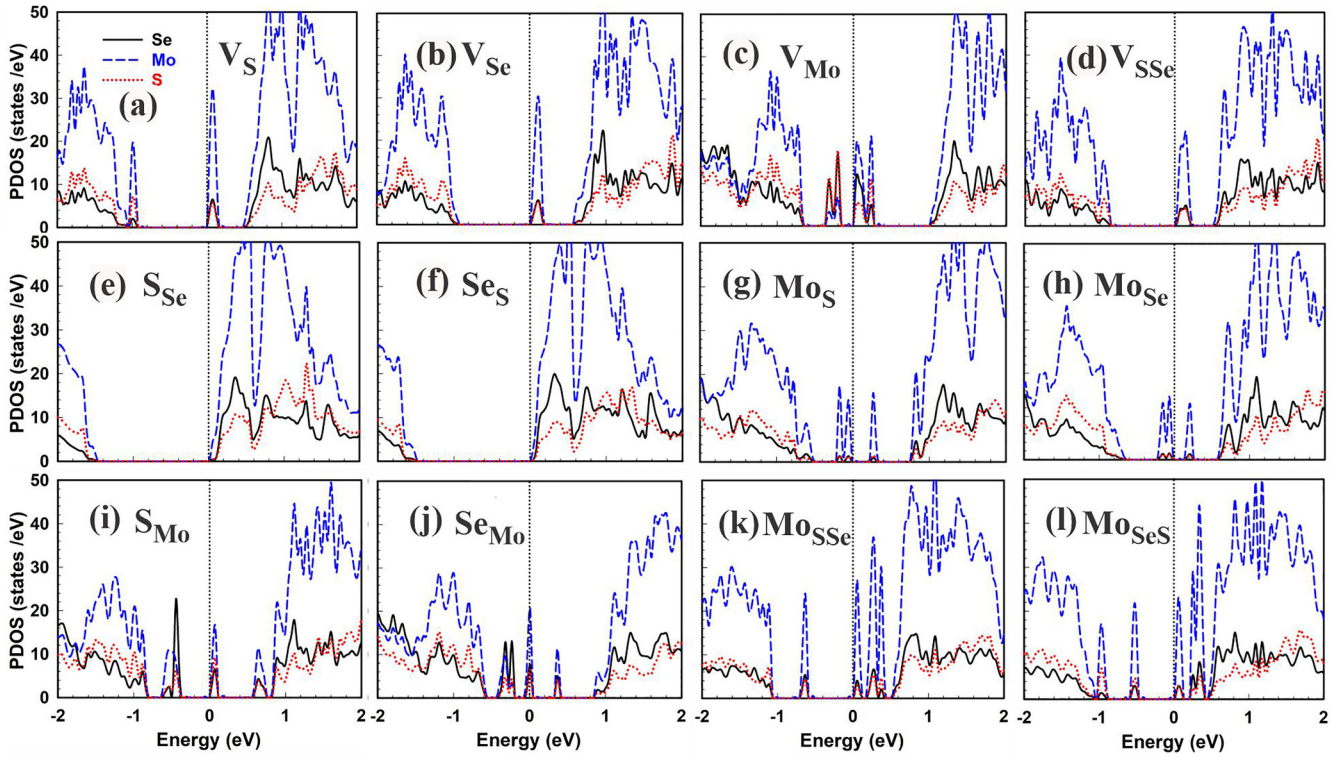

FIG. 5. Atom-projected densities of states of Janus MoSSe monolayer with defects. The solid, dashed, and dotted lines are the contributions of Se, Mo, and S atoms into the total densities of states, respectively. Here, the Fermi energy has been set to zero.

superposition of the band structures of V_S and V_{Se}. Thus, the interaction between the electronic defect states is rather weak [see Fig. 4(d)].

4. Isovalent defects

The defects S_{Se} and Se_S, which have the lowest formation energy, do not induce any defect states in the band gap. The band structures shown in Figs. 4(e) and 4(f) therefore resemble the band structure of the pure material, Fig. 3. The band gap of the pure material is almost unchanged in PBE, and slightly enlarged in HSE06, possibly due to local strain induced by the Se atom replacing the small S atom, or vice versa.

5. Mo antisite defects

When a Mo atom replaces either S or Se atom, Mo_S, Mo_{Se}, a local nonzero magnetic moment is generated at the defect site. In fact, these antisite defects favor a triplet-state configuration and some could act as defect spin qubit [25]. But, as pointed out earlier, only under low-defect concentrations (especially for Mo_S, Mo_{Se}), the local nonzero magnetic moment characteristics is observed, thus, a well-tuned defect concentration is needed for realization of a spin qubit.

When the antisite defects Mo_S and Mo_{Se} are formed, due to interactions between the antisite Mo and adjacent Mo atoms and bond formation, there are two extra electrons for each antisite Mo atom. The extra electrons occupy two defect spin-up levels in the energy gap [see Figs. 4(g) and 4(h)], thus giving rise to a triplet state. Given the C_{3v} local symmetry of structural environment surrounding the antisite Mo, its doubly degenerate $d_{x^2-y^2}$ and d_{xy} orbitals belong to a two-dimensional irreducible representation (IR) of E type, while the d_{z^2} orbital belongs to a 1D IR of A_1 type.

This symmetry classification carries over to the Mo_S or Mo_{Se} antisite defect and its midgap states. The energy difference between the E- and A_1-type states depends on the degree of hybridization between the antisite Mo and adjacent Mo atoms. The average distance between antisite Mo and adjacent Mo atom for Mo_S (2.570 Å) is smaller than for Mo_{Se} (2.594 Å), thus a larger overlap of wave functions is expected for Mo_S. The larger the wave-function overlap, the greater the level splitting. Therefore, one concludes that the lowering of the occupied $d_{x^2-y^2}$ and d_{xy} level pair due to hybridization with the neighboring Mo atoms relative to the unoccupied d_{z^2} level is greater when Mo substitutes for the S atom compared to the Se atom.

Table I shows opposite changes in the total electric dipole moment when antisite defects Mo_S and Mo_{Se} are introduced into the MoSSe structure. It is seen that the magnitude of dipole moment drops by over 50% when a single Mo atom substitutes an S anion. In contrast, dipole moment magnitude increases significantly when it substitutes a Se (see Table I) anion. To rationalize this finding, one should note that the Mo cation carries a large positive charge when incorporated into the structure. Thus, depending on its position in the structure, it adds to or subtracts from the intrinsic dipole moment of the MoSSe layer. When it resides at the top-most atomic layer (where S anions reside), the newly generated positive charge center induces a large dipole moment pointing in the $-z$ direction, opposing the total dipole moment. A positive charge center at the bottom-most layer (Mo_{Se}) acts reversely, enhancing largely the total dipole moment density per surface area.

6. S_{Mo} and Se_{Mo} antisite defects

When one Mo atom in the central atomic layer is replaced by an S or Se atom, it is found that this atom relaxed away from the high-symmetry lattice position (see Fig. 1). Substituting the Mo cation with a chalcogenide anion gives rise to a reduction of the total electric dipole moment. This seems to indicate that the polarization of the charge distribution in the central Mo atoms contributes considerably to the total dipole moment of the MoSSe layer, and replacing Mo with a less polarizable anion thus reduces the overall dipole moment.

The S_{Mo} defect gives rise to multiple midgap states. The top-most unoccupied midgap bands are mostly constructed out of the Mo ($4d$) orbitals, while the occupied defect states show anionic character, mostly from Se atoms [see Figs. 4(i) and 5(i)]. At the concentration studied here, the system remains a nonmagnetic semiconductor with a direct band gap of 0.45 eV in PBE (0.81 eV in HSE06). For Se_{Mo} calculated with the HSE06 functional, the situation is analogous to S_{Mo}, but with a smaller band gap of 0.66 eV. It is noteworthy that the PBE functional fails to open a band gap in this case. The partial filling of bands, also visible in the PDOS in Fig. 5(j), results in a magnetic ground state in the PBE calculation. Total-energy calculations with the HSE06 functional (but based on the PBE-relaxed positions) suggest that the magnetic moment persists even in the presence of a band gap.

Finally, we study defect complexes combining a Mo_S antisite with a Se vacancy on the opposite side of MoSSe layer or combing a Mo_{Se} antisite with an S vacancy on the opposite side. These defect complexes are denoted by Mo_{SSe} and Mo_{SeS}, respectively. The presence of both vacancy and antisite defects drastically changes the electronic structure of a pure MoSSe monolayer. The electronic band gap is narrowed down to 0.66 (0.54 eV) when a Mo atom lands at the S (Se) site and one Se (S) atom is detached from the atomic structure of the MoSSe monolayer (the corresponding values with the HSE06 functional are 1.17 and 1.04 eV). The band-gap narrowing occurs due to several midgap defect bands. From Figs. 5(k) and 5(l), one can find that the defect bands are constructed mainly out of $4d$ orbitals of Mo atoms. The total-energy calculations show that the ground state of both Mo_{SSe} and Mo_{SeS} has zero magnetic moment. Thus, they both possess a singlet electronic configuration (see Table I).

The zero local magnetic moment means that the four extra electrons filling the d orbitals pair up and antialign in two $4d$ orbitals, rendering a total electron spin of zero. The larger electronic band gap for Mo_{SSe} (0.67 eV) than for Mo_{SeS} (0.54 eV) reflects the stronger interaction between the antisite and surrounding Mo atoms, which results in smaller distance [46] between the antisite Mo atom with two neighboring Mo atoms in the central atomic plane.

Hence, a larger wave-function overlap with neighboring Mo atoms takes place, which in turn triggers a greater splitting of $d_{x^2-y^2}$ and d_{xy} level pair and the unoccupied d_{z^2} orbital. As a result, a slightly larger band gap is observed for Mo_{SSe}

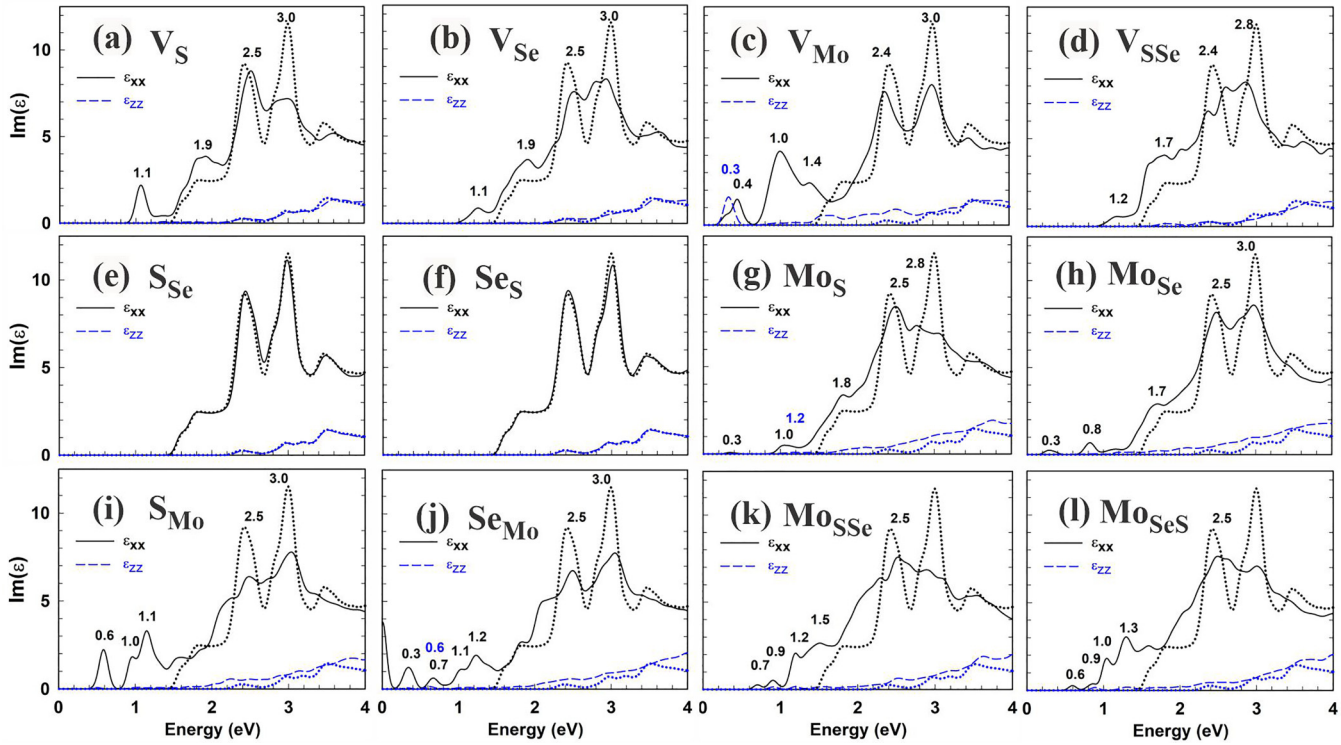

FIG. 6. In-plane (black solid line) and out-of-plane (blue dashed line) components of imaginary parts of dielectric functions of Janus MoSSe ML with point vacancy and antisite defects. For comparison, the components of the dielectric functions for pure Janus MoSSe ML are plotted using the dotted lines.

than for Mo_{SeS} (see Table I). Evaluating the total electric dipole moment density D_{tot} of the MoSSe ML with Mo_{SSe} and Mo_{SeS} defects, one can find that the D_{tot} calculated for these structures reflects the complementary changes in D_{tot} due to Mo_{Se}/Mo_{Se} and V_{Se}/V_S defects.

C. Linear optical properties of Janus MoSSe with point defects

In view of optical applications envisaged for Janus transition-metal chalcogenides, it is worth studying the linear optical properties of this type of material and the impact of the presence of the point defects on the overall linear optical response. Here, we present the results of calculations of the frequency-dependent dielectric function (and, where needed, the absorption) of the Janus MoSSe ML without and with point defects based on the electronic band structure obtained with the PBE functional. We limit the energy window up to 4.0 eV since there is a limit on describing the high-energy-lying conduction levels using an atom-centered basis expansion of Kohn-Sham wave functions. Due to the isotropy of the linear response within the plane, $\epsilon_{xx} = \epsilon_{yy}$, and it is sufficient to plot only one of both quantities.

First, we verified that the independent-particle response gives a good description of the optical properties close to the absorption threshold. For this purpose, a comparison of the calculated and measured absorption spectra (adopted from Zheng *et al.* [51]) is presented [46] both for MoS_2 and MoSSe. We find that both materials show a smooth onset of absorption below photon energies of 2 eV. At higher photon energies, a peak structure in the absorption spectrum is observed both in the measurements and in our calculations. In addition, a comparison of the calculated in-plane imaginary part of dielectric functions (ϵ_{xx}) of MoS_2, $MoSe_2$, and MoSSe [46] shows that the characteristic of MoSSe is a double-peak structure with maxima at photon energies of 2.4 and 3.0 eV.

Figure 6 shows the linear optical response of Janus MoSSe ML with vacancies and antisite defects. It is seen that for all geometries, the out-of-plane component of the imaginary part (ϵ_{zz}) is always lower in value than the in-plane component (ϵ_{xx}) for the entire energy region. This is because due to the confinement of the electrons in the z direction perpendicular to the MoSSe layer, the electronic system is less polarizable in the direction normal to the MoSSe layer as compared to polarization within the layer.

As point defects of different types can largely modify the electronic band structure of the Janus MoSSe ML, the linear optical response of monolayer MoSSe depends on the type of the dominant defect formed within it. For point defects, there are several more peaks emerging right before the prominent peaks of the pure MoSSe ML; for V_S at 1.1 eV, for V_{Se} at 1.2 eV, V_{Mo} at 0.4 eV, 1.0 eV, and 1.4 eV, and for V_{SSe} 1.2 eV. The emergence of these peaks suggests that electronic transitions from the valence band edge to midgap energy states as well as between midgap states can take place. As we stated earlier, for Janus MoSSe ML with V_{Mo} defect, the midgap occupied electronic bands possess mostly p (of Se and S atoms) character, while the occupied electronic bands have a mixed character of p and d orbitals [see Fig. 5(c)]. Figure 6(c) shows the in-plane and out-of plane optical response of Janus MoSSe ML with a Mo vacancy. Two small peaks are seen at 0.3 and 0.4 eV in ϵ_{xx} and ϵ_{zz}, respectively, which can be attributed to a low-energy transition between

only the midgap states. To put this into more context, from the atom-resolved densities of states [Fig. 5(c)] one can find that the low-energy peak in ϵ_{xx} is due to the *p*-*d* transitions between orbitals in the plane, while the prominent peak in ϵ_{zz} is attributed to a transition between p_z orbitals of Se atoms and d_{z^2} orbitals of adjacent Mo atoms. For V_S, V_{Se}, and V_{SSe} the low-energy transitions occur from the valence band to unoccupied midgap states, or between midgap electronic orbitals all of 4*d* character of Mo atoms surrounding the vacant site [see Figs. 6(a), 6(b), and 6(d)].

For the isovalent chalcogenide antisite defects S_{Se} and Se_S, there is little change in the optical response compared to the perfect MoSSe layer, as seen from Figs. 6(e) and 6(f). Thus, optical measurement could not be an effective tool to identify the formation of such defect within the Janus MoSSe. In particular, the double-peak structure at 2.4 and 3.0 eV is retained.

In contrast to these defects, substituting one chalcogen atom with the transition-metal atom (Mo) or vice versa could largely change the linear optical response of the Janus MoSSe. A number of new peaks emerge before the "signature" peaks of Janus MoSSe ML at 2.4 and 3.0 eV when such defects are introduced into the MoSSe monolayer structure. There are two extra peaks emerging at 0.2 and 1.0 eV for Mo_S [see Fig. 6(g)]. The former is attributed to the transition between midgap energy levels constructed mainly out of Mo *d* orbitals, while the latter is attributed to the transition between the occupied midgap and conduction energy levels, which are also of *d* character [see Fig. 5(g)]. Similar pattern is observed for Mo_{Se}, where transitions occur at 0.2 and 1.0 eV [see Fig. 6(h)]. The three low-intensity peaks at 0.6, 0.9, and, 1.2 eV for S_{Mo} [Fig. 6(i)] are indicative of excitation from low-density energy levels in the midgap region. In the case of Se_{Mo} [Fig. 6(j)], one can find a new peak at zero energy in the optical spectrum. The emergence of this peak reflects the intraband electronic transition of the midgap energy bands crossing the Fermi energy level, which turns the Janus MoSSe semiconductor into a semimetal. The change in the optical spectrum proves the change in the electrical conductivity of MoSSe upon replacing the transition-metal atom (at the central layer) with the heavier chalcogenide atom.

Moreover, the small peak in ϵ_{zz} at 0.6 eV [Fig. 6(j)] reflects the transition between Se p_z orbitals with spatial extension perpendicular to the MoSSe plane.

For Janus MoSSe monolayer with Mo_{SSe} and Mo_{SeS} defects, the defect-induced energy-level transitions occur between the energy levels with major Mo 4*d* orbital contributions [see Figs. 6(k) and 6(l)]. The small peaks at 0.9 and 1.2 eV (0.9 and 1.3 eV) in ϵ_{zz} of Mo_{SSe} (Mo_{SeS}) can be attributed to transition between the 4*d* orbitals extended normal to the MoSS ML plane (d_{xz} or d_{yz} and d_{z^2}).

D. Phonon spectra of defect geometries

In our calculations using the PBE functional of the vibrational spectra of all relaxed geometries, no imaginary frequencies were encountered, except a few very small imaginary frequencies (below 50 cm^{-1}) for the Mo vacancy defect. The absence of imaginary frequencies indicates that the relaxed MoSSe MLs with point defects are dynamically stable structures.

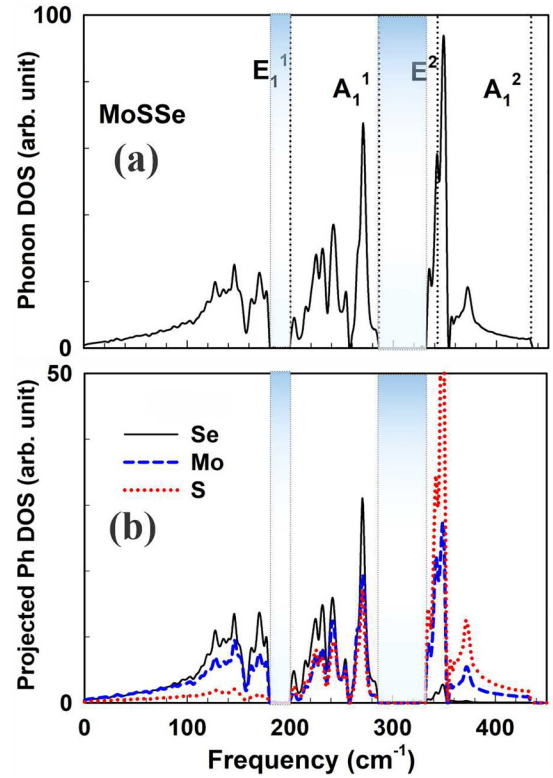

FIG. 7. Total (a) and atom-projected (b) phonon densities of states of pure Janus MoSSe ML. Four main phonon modes, E^1, A_1^1, E^2, and A_1^2, at frequencies 204, 282, 349, and 430 cm^{-1}, respectively, regarded as the fingerprints of MoSSe monolayer, have been indicated in the spectrum by the dotted line in (a). The gap region is shaded with light blue color.

1. Pure MoSeS

Similar to MoS_2, pure MoSSe possesses phonon modes that are first-order Raman active, labeled E^1, A_1^1, E^2, and A_1^2, which occur at frequencies of 200.1, 281.0, 343.6, and 429.2 cm^{-1}, respectively [see the dotted vertical lines in Fig. 7(a)]. According to group theory, the two-dimensional *E* representations and the one-dimensional A_1 representations correspond to in-plane and out-of-plane optical vibrations [23,51]. To determine the quoted frequencies, we extract the crossing point of the respective phonon bands with the Γ point [46]. Note that the Raman-active modes are usually located at phonon band edges at the Γ point of the phonon Brillouin zone, while we plotted the phonon density of states integrated over the *entire* Brillouin zone in Fig. 7(a). Owing to the mass effect, the higher-frequency optical modes correspond to relative motions (in plane and out of plane) of the Mo atoms and the lighter chalcogen, the S atoms. In contrast, the lower-frequency optical and acoustic modes correspond to vibrations of all constituting elements of the Janus MoSSe ML [see Fig. 7(b)], while the contributions from the heavier atoms (Mo and Se) are much larger than from the lightest atoms, the S atoms. In contrast to MoS_2 and $MoSe_2$, however, the different masses on MoSSe result in *two* reststrahlen ranges

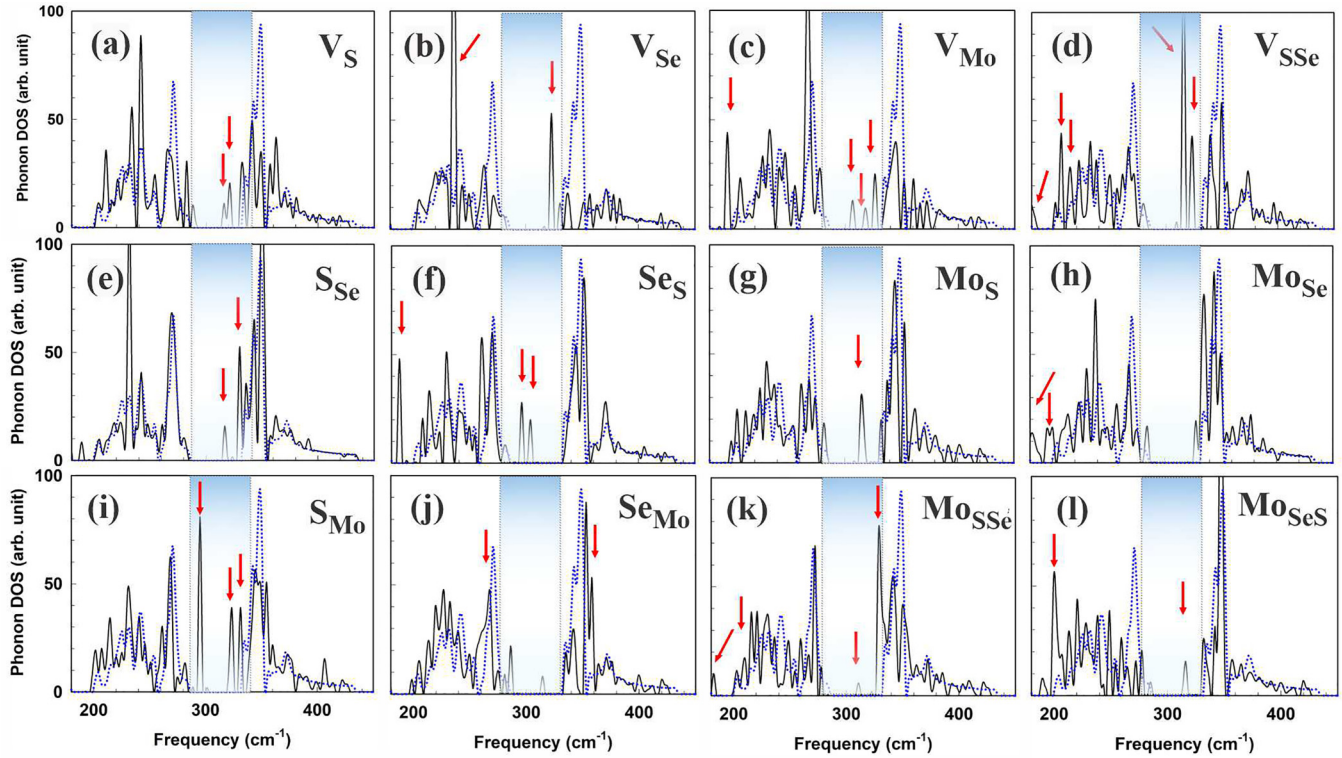

FIG. 8. Phonon densities of states of Janus MoSSe ML with point vacancy and anti-site defects. The phonon densities of states of pure MoSSe ML is given as a reference by the dotted blue line. The new peaks due to the defects are indicated by arrows. The gap region is shaded with light blue color.

(i.e., gaps in the DOS from 180 to 199 cm^{-1} and from 286 to 331 cm^{-1}, light blue shaded regions in Fig. 7) rather than just one, as found in the single-chalcogen compounds.

Figure 8 gives an overview of the phonon densities of states of all vacancies and antisite defects computed for a Janus MoSSe (4×4) supercell. In the following discussion, we disregard the spectral range of the acoustic phonons below 180 cm^{-1} because they are Raman inactive and remain almost unchanged upon introducing the structural defects. In Fig. 8 we emphasize the comparison to the spectrum of defect-free MoSSe. In order to identify the origin of localized modes, we also calculated atom-projected densities of states of the phonons that are provided in Fig. 9. As a general observation, when the point-vacancy defects are formed, new peaks appear in the reststrahlen gap (light blue shaded regions), indicative of vibrations localized at the defect site. From analyzing the phonon band structure in the (4×4) supercell [46] and comparing to the band structure of the (1×1) supercell, we are able to follow the Raman-active modes in the presence of a defect. We note that most defects (those shown in the first two rows of Fig. 1) retain the C_{3v} symmetry, and consequently the classification of the Raman modes into E and A modes remains to be valid in these cases.

2. *Vacancies*

Table II shows in the second column the frequency shift of the Raman-active modes, while in the third column the location of new peaks emerging in the phonon spectrum of the Janus MoSSe ML due to the introduction of defects is listed.

For example, removing one S atom (V_S) introduces peaks at 316 and 321 cm^{-1} [marked by arrows in Fig. Fig. 8(a)] that are split off from the highest optical phonon branches. The analysis with the help of the atom-projected DOS tells us that the localized vibrations due to the S vacancy mainly originate from the nearby S atoms (n-S). This is because surface stress is relieved by V_S, and hence the force constants for nearby S atoms are reduced. Apart from this, V_S does not perturb the MoSSe vibrations too much, as it is clearly understood from the persistence of the main pristine MoSSe peak at 343 cm^{-1} [see Fig. 8(a)]. However, the A_1^1 peak is shifted downward from 286 to 281 cm^{-1}. In contrast, when V_{Se} is formed, the vibrational spectrum is more strongly perturbed, such that the main peaks in the DOS are largely overshadowed by a relatively strong defect-induced peak in the gap region [see Fig. 8(b)]. The coexistence of diminished main peaks and the emergence of a new peak in the reststrahlen gap indicate a localized vibration due to major structural deformation caused by the missing Se atom (the 4% reduction in the distances between Mo atoms surrounding the V_{Se} site) with a larger mass (than the mass of the S atom). The sharp resonance at 236 cm^{-1} visible in Fig. 8(b) can be assigned to collective vibrations of the nearby Se atoms (n-Se) surrounding the Se vacancy site. The peak at 323 cm^{-1} inside the gap is due to the vibrations of undercoordinated Mo atoms surrounding the defect site and light S atoms at the opposite side of the MoSSe layer.

Removing Mo atoms or two chalcogenide atoms (one from each side) also gives rise to the emergence of some new peaks in the vibration gap [see Figs. 8(c) and 8(d)]. In the case of

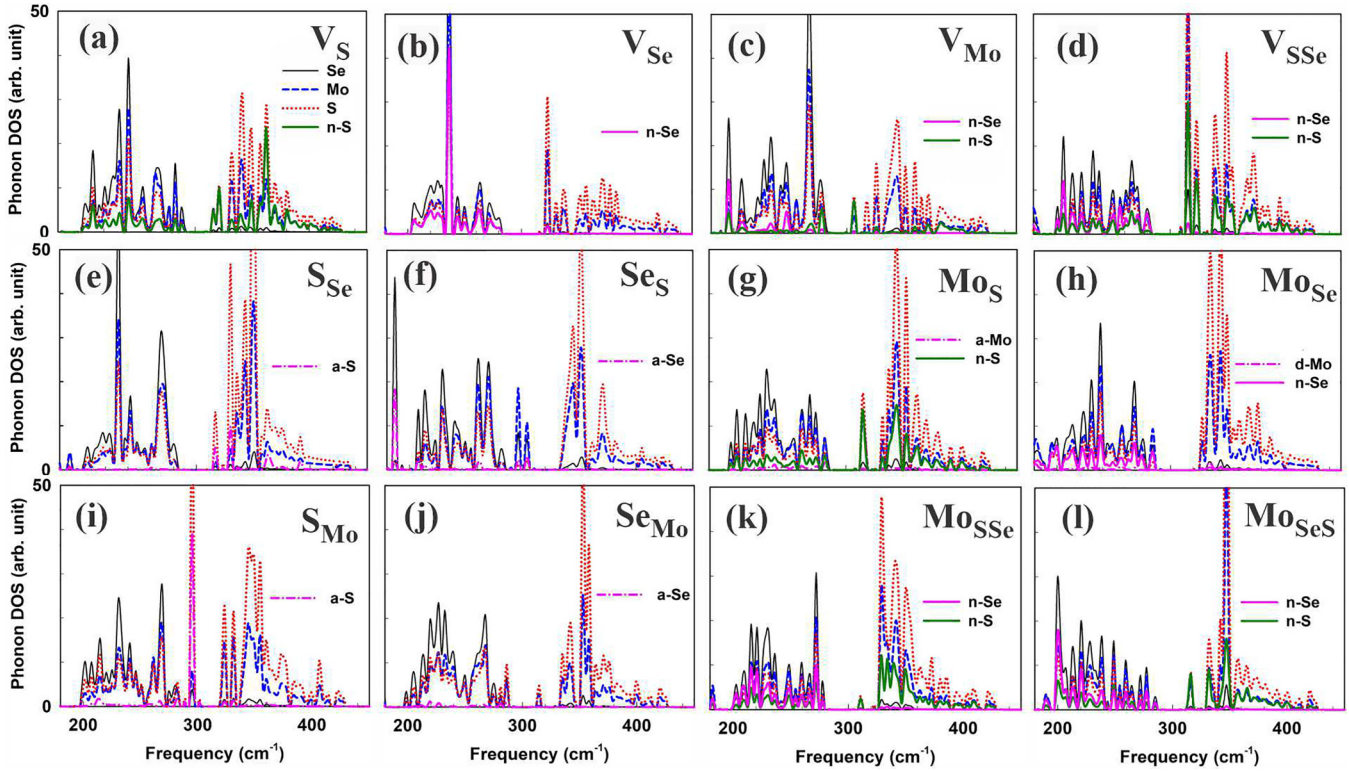

FIG. 9. Projected phonon densities of states of Janus MoSSe ML with point-vacancy and antisite defects. The black solid, blue dashed, and red dotted lines correspond to Se, Mo, and S atoms, respectively. The contribution into the total phonon densities of states from the antisite element atoms are indicated by a- before the atom type. Also, the contributions to phonon density of states from the Se and S atoms near a (vacancy or antisite) defect site (n-Se and n-S) are indicated by the n- before each nearby atom.

V_{Mo}, the new peaks emerged (at 307, 319, and 326 cm^{-1}) in the phonon gap are smaller than the prominent E^2 peak and mostly originate from the light S atoms adjacent to the missing-Mo-atom site.

A new peak emerged below 200 cm^{-1} can be assigned to in-plane vibration ($E_1^{1'}$) of undercoordinated heavy Se atoms. The atom-projected phonon densities of states for nearby Se atoms prove such an assignment [see Fig. 9(c)].

Contrary to V_{Mo}, for V_{SSe}, the defect peaks at 316 and 324 are very large and overshadowing the prominent peaks of the MoSSe ML [see Fig. 8(d)]. Also, there are several new peaks in the low-frequency range of optical modes, such as the peaks at 179, 206, and 214 cm^{-1}. As can be seen from Fig. 9(d), these new peaks can be assigned to the softened vibrations of the three undercoordinated Mo atoms between the S and Se vacancy sites. The vibrations of the S and Se atoms adjacent

TABLE II. The frequencies of the Raman-active modes (second column) for Janus MoSSe ML without and with point defects. Also, the frequencies at which new peaks emerge due to the formation of point defects are given (third column). The change in the average phonon frequency ($\Delta\bar{\omega}_{ave}$) due to the formation of the point defect is given in the third column. Here, for pure Janus MoSSe $\bar{\omega}_{ave} = 241.41$ cm^{-1}.

Structure	Raman modes (cm^{-1})	Defect peaks (cm^{-1})	$\Delta\bar{\omega}_{ave}$ (cm^{-1})
MoSSe	200, 286, 343, 433		0
V_S	202, 281, 344, 427	211, 282, 288, 316, 321	−11.4
V_{Se}	202, 283, 345, 437	323, 331	−23.2
V_{Mo}	205, 281, 344, 424	196, 307, 319, 326	−21.7
V_{SSe}	199, 284, 342, 426	206, 316, 324	−6.3
S_{Se}	202, 283, 343, 435	189, 231, 317, 323, 330, 362, 391	6.6
Se_S	206, 283, 343, 432	187, 214, 260, 296, 304	−3.8
Mo_S	204, 284, 342, 425	314, 362	−10.3
Mo_{Se}	205, 280, 342, 429	182, 201	−5.0
S_{Mo}	200, 281, 343, 428	295, 323, 331	−3.4
Se_{Mo}	201, 286, 343, 426	198, 285, 314	−15.7
Mo_{SSe}	200, 279, 342, 427	183, 208, 311, 328	−6.5
Mo_{SeS}	200, 280, 343, 426	190, 200, 316	−16.2

to the S and Se vacancy sites also contribute to the emergence of new peaks at high and low frequencies, respectively.

3. Isovalent defects

Earlier we showed that isovalent substitution does not make a significant change in the electronic band structure of the Janus MoSSe [see Figs. 5(e) and 5(f)]. But, such substitution could have some fingerprints left in the vibration spectrum of Janus MoSSe ML. Figures 8(e) and 8(f) display the changes in the spectra upon formation of S_{Se} and Se_S antisite defects, respectively. For S_{Se} the peaks in the upper reststrahlen gap at 317, 323, and 330 cm^{-1} are due to the light S atom introduced into a Se lattice site. In addition, there are two new peaks above 360 cm^{-1} having antisite S atom character, as can be seen from Fig. 9(e). One would expect that the average phonon frequency ($\bar{\omega}_{ave}$) should shift to higher frequencies when a heavy element in the structures is substituted by a lighter element in the same group of the periodic table. The larger $\bar{\omega}_{ave}$ calculated for S_{Se} confirms such prediction (see Table II).

Contrary to the case of S_{Se}, when the heavier chalcogenide atom (Se atom) substitutes the lighter chalcogenide atom (S atom), the changes in the phonon spectrum mostly take place in the low-frequency region of optical phonon spectrum (the optical gap and nongap region) of MoSSe ML. This can be clearly seen in the phonon densities of states of Janus MoSSe ML with defect Se_S [see Fig. 8(f)]. Two new midgap peaks emerge at 296 and 304 cm^{-1} in the upper reststrahlen gap. They mainly originated from the Se and Mo atoms as well as the antisite Se atom residing at the S-atom side of the MoSSe ML [cf. Fig. 9(f)]. A newly emerged peak below frequency 200 cm^{-1} is mainly originated from the heavy Se atoms, especially the antisite Se atom.

The changes in the low-frequency region of the vibration spectrum reflect the fact that a heavier antisite atom in the lattice generates vibrations with lower frequencies. The redshift of the average phonon frequency ($\bar{\omega}_{ave}$) calculated for Se_S clearly reflects this mass effect. Finally, it must be noted that although replacing one chalcogen with the other does not bear any significant changes in the electronic structure of Janus MoSSe, it leaves some visible fingerprints in MoSSe phonon spectrum in the region which is usually probed by Raman spectroscopy [23].

4. Mo antisite defects

Formation of Mo antisite defects (Mo_S and Mo_{Se}) with large formation energies may occur under nonequilibrium growth conditions, as usually encountered in thermal synthesis processes, such as chemical vapor deposition [22]. Given the large structural changes, these defect types introduce into the MoSSe ML (see Table I), strong changes in the phonon vibration spectrum of MoSSe ML are expected. Depending on the type of chalcogen atom a Mo atom substitutes, the change can occur in different (low- or high-frequency) regions of the vibration spectrum. The presence of a Mo atom at each side of MoSSe facilitates stronger hybridization of 4*d* orbitals of the antisite Mo atom and nearby Mo atoms (due to the formation of covalent bonds between). The new covalent bonds largely reduce the distance between Mo atoms in the vicinity of the defect site. This can also affect the in-plane vibrations of the surrounding chalcogen atoms, inducing low- or high-frequency phonon modes into the vibrational spectrum. Figures 8(g) and 8(h) display the phonon densities of states of Janus MoSSe with Mo_S and Mo_{Se} defects. Mo_S induces a high-frequency peak at 314 cm^{-1} in the gap [Fig. 8(g)], whereas Mo_{Se} generates mostly new low-frequency vibrations (182 and 201 cm^{-1}) in the spectrum [Fig. 8(h)]. Looking at the atom-projected phonon densities of states [Figs. 9(h) and 9(g)], one can see that the new vibrations occur due to distorted in-plane motions of chalcogen atoms surrounding the antisite Mo atom.

Since the mass of transition-metal atom Mo is larger than the mass of both chalcogens, one expects a reduction in the average phonon frequency ($\bar{\omega}_{ave}$) of the Janus MoSSe ML. However, depending on the mass of the chalcogen replaced, the magnitude of the $\bar{\omega}_{ave}$ reduction varies. In accordance with the mass effect, the $\bar{\omega}_{ave}$ shift to lower frequencies is larger for Mo_S than Mo_{Se} since a smaller mass (of S) is replaced with the larger mass of the Mo atom.

5. S_{Mo} and Se_{Mo} antisite defects

While the Mo antisites considered above introduce isotropic structural changes, substituting Mo in the central layer with a chalcogen anisotropically modifies the MoSSe structure. The chalcogen antisite atom is attracted unequally by the surrounding Mo and chalcogen atoms owing to fewer orbitals available for the chalcogens. A new phonon mode at 295 cm^{-1} emerges [shown in Fig. 8(i)] when one sulfur atom replaces one Mo atom, S_{Mo}. The assignment is attributed to out-of-plane vibrations of the antisite light S atom relative to the adjacent atoms [see Fig. 9(i)]. Moreover, upon introducing the Se_{Mo} some optical phonon modes (at 357 cm^{-1}) shift to higher frequencies, as seen in Fig. 8(j). This can be explained by the fact that when one Se atom substitutes one Mo atom (in the central plane), the bonds between the S/Se atom (at both sides) and the antisite Se atom, as well as the two bonds between two neighboring Mo atoms and antisite Se are contracted by 2.3% and 13.0%, respectively. The bond contractions give rise to an increase in the frequency of the phonon mode. Contrary to this, some phonon modes [like the peak centered at 270 cm^{-1}, which is indicated by an arrow in Fig. 8(j)] shift to lower frequencies due to weakening the bond between the antisite Se atom and one Mo atom in the central plane. Similar to the vacancy case, breaking or weakening some bonds due to fewer orbitals available for the antisite chalcogen atoms leads to vibrational modes that get softer or disappear completely. As a result, the average phonon frequency of the Janus MoSSe is decreased. The reduction is smaller for S_{Mo} than Se_{Mo} since the lighter S atom substitutes a heavy Mo atom.

We now turn to the defect complexes Mo_{SSe}, which are the combination of vacancy and antisite defect at a single atomic column. The defect peaks at low- (183 and 208 cm^{-1}) and high- (311 and 328 cm^{-1}) frequency regions for Mo_{SSe} are due to the in-plane nearby S and Se atom vibrations perturbed due to presence of the Mo atom and absence of Se, respectively [see Fig. 8(k)]. A very similar pattern is observed for MoSSe with Mo_{SeS} defect for low-frequency defect-induced

vibrations at 190 and 200 cm^{-1}, while the high-frequency vibration emerges at 316 cm^{-1} [see Fig. 8(l)]. Atom-project phonon densities of states in Fig. 9(l) suggest that the low-frequency defect peaks can be attributed to the perturbed low-frequency (in-plane) vibration of Se atoms surrounding the Mo_{Se} site. Also, one missing S atom at the other side of MoSSe ML gives rise to inward-vacancy-region motion of the nearby S atoms (n-S), distorting the symmetry of the binding to adjacent Mo atoms. Thus, a new high-frequency vibration emerges at 316 cm^{-1}, which is assigned to the perturbed vibration of n-S.

Finally, we believe that the presented vibration analyses will provide fundamental information on which vibration fingerprints (specific phonon mode feature) can be observed in Raman spectroscopy of Janus MoSSe ML when a certain type of defect dominates, which may be correlated to specific experimental growth condition.

IV. CONCLUSIONS

Using density functional theory, we have studied thermal stability, electronic structure, linear optical properties, and the vibration spectrum of a Janus MoSSe monolayer with commonly encountered point-vacancy and antisite defects. It is found that the isovalent substitution of sulfur by selenium and vice versa has the lowest formation energy but does not lead to electronic states inside the band gap. However, experimental detection of these defects is possible via infrared or Raman spectroscopy due to their unique vibrational features. All other defects studied induce deep levels in the band gap. Moreover, our calculations show that the defect-induced changes in the electronic structure translate into characteristic features in the linear optical spectrum of the Janus MoSSe monolayer. In the case of antisite chalcogenide atoms, upon replacing Mo with Se, a transition to a semimetal is observed for the defect concentration assumed in our calculations. Our total-energy calculations, with both semilocal and hybrid exchange-correlation functionals, reveal that the point-vacancy defects carry no total spin magnetic moment. However, Mo antisite defects are found to possess a nonzero magnetic moment as long as their concentrations are low. The calculations of vibrational spectra for all defects reveal that each defect leaves unique fingerprints in the Janus MoSSe phonon spectrum.

In view of possible applications of the material, we note that the characteristic spin-orbit-split conduction band valley is retained even with defects, which renders the Janus MoSSe monolayer a suitable candidate for optoelectronic and spintronic applications. In determining the suitability of the Janus MoSSe surface for catalysis applications, the magnitude and direction of the total electric dipole moment vector have pivotal roles. A stronger dipole moment oriented in the right direction can steer a charge-polarized molecule, such as a water molecule, toward the surface, making effective molecular adsorption feasible. Therefore, we believe that the analysis of defect-induced changes in the electric dipole carried out in this work can aid researchers in envisaging suitable materials design for enhancing one specific chemical process. Investigating the influence of the Janus MoSSe dipole moment on the overall water-splitting process (as the central pillar of the chemical-to-electric energy conversion mechanism) on the MoSSe ML surface can be an intriguing unexplored area left for future research.

ACKNOWLEDGMENTS

This research is funded by the Deutsche Forschungsgemeinschaft (DFG, German Research Foundation) through Project No. B02 of Collaborative Research Center SFB1242 "Nonequilibrium dynamics of condensed matter in the time domain" (Project No. 278162697). The authors also gratefully acknowledge the funding of this project by computing time provided by the Paderborn Center for Parallel Computing (PC2) project hpc-prf-seer. We would like to thank Zheng *et al.* [51] for kindly sharing the results of their optical measurements.

H.M. performed DFT and postprocessing calculations. P.K. conceived and supervised the project. The manuscript was written through the contributions of both authors.

The authors declare to have no competing financial interests.

[1] K. F. Mak and J. Shan, Photonics and optoelectronics of 2D semiconductor transition metal dichalcogenides, Nat. Photonics **10**, 216 (2016).

[2] M. Samadi, N. Sarikhani, M. Zirak, H. Zhang, H.-L. Zhang, and A. Z. Moshfegh, Group 6 transition metal dichalcogenide nanomaterials: Synthesis, applications and future perspectives, Nanoscale Horizons **3**, 90 (2018).

[3] Q. Yun, L. Li, Z. Hu, Q. Lu, B. Chen, and H. Zhang, Layered transition metal dichalcogenide-based nanomaterials for electrochemical energy storage, Adv. Mater. **32**, 1903826 (2020).

[4] Y. Ye, J. Xiao, H. Wang, Z. Ye, H. Zhu, M. Zhao, Y. Wang, J. Zhao, X. Yin, and X. Zhang, Electrical generation and control of the valley carriers in a monolayer transition metal dichalcogenide, Nat. Nanotechnol. **11**, 598 (2016).

[5] X. Xu, W. Yao, D. Xiao, and T. F. Heinz, Spin and pseudospins in layered transition metal dichalcogenides, Nat. Phys. **10**, 343 (2014).

[6] M. Meng, T. Li, S. Li, and K. Liu, Ferromagnetism induced by point defect in Janus monolayer MoSSe regulated by strain engineering, J. Phys. D: Appl. Phys. **51**, 105004 (2018).

[7] A.-Y. Lu, H. Zhu, J. Xiao, C.-P. Chuu, Y. Han, M.-H. Chiu, C.-C. Cheng, C.-W. Yang, K.-H. Wei, Y. Yang *et al.*, Janus monolayers of transition metal dichalcogenides, Nat. Nanotechnol. **12**, 744 (2017).

[8] Y. Wei, X. Xu, S. Wang, W. Li, and Y. Jiang, Second harmonic generation in Janus MoSSe a monolayer and stacked bulk with vertical asymmetry, Phys. Chem. Chem. Phys. **21**, 21022 (2019).

[9] N. Abidi, A. Bonduelle-Skrzypczak, and S. N. Steinmann, Revisiting the active sites at the MoS_2/H_2O interface via grand-canonical DFT: The role of water dissociation, ACS Appl. Mater. Interfaces **12**, 31401 (2020).

[10] Q. Xiong, Y. Wang, P.-F. Liu, L.-R. Zheng, G. Wang, H.-G. Yang, P.-K. Wong, H. Zhang, and H. Zhao, Cobalt covalent doping in MoS_2 to induce bifunctionality of overall water splitting, Adv. Mater. **30**, 1801450 (2018).

[11] S. Tao, B. Xu, J. Shi, S. Zhong, X. Lei, G. Liu, and M. Wu, Tunable dipole moment in Janus single-layer MoSSe via transition-metal atom adsorption, J. Phys. Chem. C **123**, 9059 (2019).

[12] J. Zhang, S. Jia, I. Kholmanov, L. Dong, D. Er, W. Chen, H. Guo, Z. Jin, V. B. Shenoy, L. Shi *et al.*, Janus monolayer transition-metal dichalcogenides, ACS Nano **11**, 8192 (2017).

[13] C. T. Le, D. J. Clark, F. Ullah, J. I. Jang, V. Senthilkumar, Y. Sim, M.-J. Seong, K.-H. Chung, J. W. Kim, S. Park *et al.*, Impact of selenium doping on resonant second-harmonic generation in monolayer MoS_2, ACS Photonics **4**, 38 (2017).

[14] S.-B. Yu, M. Zhou, D. Zhang, and K. Chang, Spin Hall effect in the monolayer Janus compound MoSSe enhanced by Rashba spin-orbit coupling, Phys. Rev. B **104**, 075435 (2021).

[15] M. C. Lucking, K. Beach, and H. Terrones, Large second harmonic generation in alloyed TMDs and boron nitride nanostructures, Sci. Rep. **8**, 10118 (2018).

[16] Y. Cheng, Z. Zhu, M. Tahir, and U. Schwingenschlögl, Spin-orbit-induced spin splittings in polar transition metal dichalcogenide monolayers, Europhys. Lett. **102**, 57001 (2013).

[17] L. Ju, M. Bie, J. Shang, X. Tang, and L. Kou, Janus transition metal dichalcogenides: A superior platform for photocatalytic water splitting, J. Phys. Mater. **3**, 022004 (2020).

[18] J. Schmeink, V. Musytschuk, E. Pollmann, S. Sleziona, A. Maas, and M. Schleberger, Lifetime of excitons in Janus monolayer MoSSe prepared from exfoliated $MoSe_2$, arXiv:2112.11211.

[19] H.-P. Komsa and A. V. Krasheninnikov, Native defects in bulk and monolayer MoS_2 from first principles, Phys. Rev. B **91**, 125304 (2015).

[20] K. Zhang, Y. Guo, Q. Ji, A.-Y. Lu, C. Su, H. Wang, A. A. Puretzky, D. B. Geohegan, X. Qian, S. Fang, E. Kaxiras, J. Kong, and S. Huang, Enhancement of van der Waals interlayer coupling through polar Janus MoSSe, J. Am. Chem. Soc. **142**, 17499 (2020).

[21] W. Zhou, X. Zou, S. Najmaei, Z. Liu, Y. Shi, J. Kong, J. Lou, P. M. Ajayan, B. I. Yakobson, and J.-C. Idrobo, Intrinsic structural defects in monolayer molybdenum disulfide, Nano Lett. **13**, 2615 (2013).

[22] J. Hong, Z. Hu, M. Probert, K. Li, D. Lv, X. Yang, L. Gu, N. Mao, Q. Feng, L. Xie *et al.*, Exploring atomic defects in molybdenum disulphide monolayers, Nat. Commun. **6**, 6293 (2015).

[23] M. M. Petrić, M. Kremser, M. Barbone, Y. Qin, Y. Sayyad, Y. Shen, S. Tongay, J. J. Finley, A. R. Botello-Méndez, and K. Müller, Raman spectrum of Janus transition metal dichalcogenide monolayers WSSe and MoSSe, Phys. Rev. B **103**, 035414 (2021).

[24] A. Kandemir and H. Sahin, Bilayers of Janus WSSe: Monitoring the stacking type via the vibrational spectrum, Phys. Chem. Chem. Phys. **20**, 17380 (2018).

[25] J.-Y. Tsai, J. Pan, H. Lin, A. Bansil, and Q. Yan, Antisite defect qubits in monolayer transition metal dichalcogenides, Nat. Commun. **13**, 492 (2022).

[26] S. Gupta, J.-H. Yang, and B. I. Yakobson, Two-level quantum systems in two-dimensional materials for single photon emission, Nano Lett. **19**, 408 (2019).

[27] H. Jin, T. Wang, Z.-R. Gong, C. Long, and Y. Dai, Prediction of an extremely long exciton lifetime in a Janus-MoSTe monolayer, Nanoscale **10**, 19310 (2018).

[28] V. Blum, R. Gehrke, F. Hanke, P. Havu, V. Havu, X. Ren, K. Reuter, and M. Scheffler, Ab initio molecular simulations with numeric atom-centered orbitals, Comput. Phys. Commun. **180**, 2175 (2009).

[29] J. P. Perdew, J. A. Chevary, S. H. Vosko, K. A. Jackson, M. R. Pederson, D. J. Singh, and C. Fiolhais, Atoms, molecules, solids, and surfaces: Applications of the generalized gradient approximation for exchange and correlation, Phys. Rev. B **46**, 6671 (1992).

[30] R. Fletcher, *Practical Methods of Optimization*, 2nd ed. (Wiley, New York, 1987).

[31] J. D. Pack and H. J. Monkhorst, "Special points for Brillouin-zone integrations"—a reply, Phys. Rev. B **16**, 1748 (1977).

[32] W. P. Huhn and V. Blum, One-hundred-three compound band-structure benchmark of post-self-consistent spin-orbit coupling treatments in density functional theory, Phys. Rev. Mater. **1**, 033803 (2017).

[33] H.-P. Komsa, N. Berseneva, A. V. Krasheninnikov, and R. M. Nieminen, Charged Point Defects in the Flatland: Accurate Formation Energy Calculations in Two-Dimensional Materials, Phys. Rev. X **4**, 031044 (2014).

[34] C. Freysoldt, A. Mishra, M. Ashton, and J. Neugebauer, Generalized dipole correction for charged surfaces in the repeated-slab approach, Phys. Rev. B **102**, 045403 (2020).

[35] C. G. Van de Walle and A. Janotti, Advances in electronic structure methods for defects and impurities in solids, Phys. Status Solidi B **248**, 19 (2011).

[36] A. Togo and I. Tanaka, First-principles phonon calculations in materials science, Scr. Mater. **108**, 1 (2015).

[37] J. P. Perdew, K. Burke, and M. Ernzerhof, Generalized Gradient Approximation Made Simple, Phys. Rev. Lett. **77**, 3865 (1996).

[38] J. P. Perdew and A. Zunger, Self-interaction correction to density-functional approximations for many-electron systems, Phys. Rev. B **23**, 5048 (1981).

[39] J. Heyd, G. E. Scuseria, and M. Ernzerhof, Hybrid functionals based on a screened coulomb potential, J. Chem. Phys. **118**, 8207 (2003).

[40] N. Wakabayashi, H. G. Smith, and R. M. Nicklow, Lattice dynamics of hexagonal MoS_2 studied by neutron scattering, Phys. Rev. B **12**, 659 (1975).

[41] A. Roy, H. C. P. Movva, B. Satpati, K. Kim, R. Dey, A. Rai, T. Pramanik, S. Guchhait, E. Tutuc, and S. K. Banerjee, Structural and electrical properties of $MoTe_2$ and $MoSe_2$ grown by molecular beam epitaxy, ACS Appl. Mater. Interfaces **8**, 7396 (2016).

[42] Z. Wang, 2H → 1T? phase transformation in janus monolayer MoSSe and MoSTe: An efficient hole injection contact for 2H-MoS2, J. Mater. Chem. C **6**, 13000 (2018).

[43] R. Chaurasiya and A. Dixit, Defect engineered MoSSe Janus monolayer as a promising two dimensional material for NO_2 and NO gas sensing, Appl. Surf. Sci. **490**, 204 (2019).

[44] D. Edelberg, D. Rhodes, A. Kerelsky, B. Kim, J. Wang, A. Zangiabadi, C. Kim, A. Abhinandan, J. Ardelean, M. Scully, D. Scullion, L. Embon, R. Zu, E. J. G. Santos, L. Balicas, C. Marianetti, K. Barmak, X. Zhu, J. Hone, and A. N. Pasupathy, Approaching the intrinsic limit in transition metal diselenides via point defect control, Nano Lett. **19**, 4371 (2019).

[45] X. Yin, Y. Wang, R. Jacobs, Y. Shi, I. Szlufarska, D. Morgan, and X. Wang, Massive vacancy concentration yields strong room-temperature ferromagnetism in two-dimensional ZnO, Nano Lett. **19**, 7085 (2019).

[46] See Supplemental Material at http://link.aps.org/supplemental/10.1103/PhysRevB.106.235414 for (a) Table S1 for total energies of point defects in different magnetic states; (b) Table S2 for partial atomic charges; (c) Figs. S5 and S6 for orbital-resolved densities of state; (d) Figs. S1 to S4 for zoomed plots of the band structures; (e) Fig. S7 for quantitative information about the relaxed geometries; (f) Figs. S8 and S9 for dielectric functions and optical absorption spectra of the pristine materials; (g) Fig. S10 for phonon band structures.

[47] L. Cai, J. He, Q. Liu, T. Yao, L. Chen, W. Yan, F. Hu, Y. Jiang, Y. Zhao, T. Hu, Z. Sun, and S. Wei, Vacancy-induced ferromagnetism of MoS_2 nanosheets, J. Am. Chem. Soc. **137**, 2622 (2015).

[48] H. Zheng, B. Yang, D. Wang, R. Han, X. Du, and Y. Yan, Tuning magnetism of monolayer MoS_2 by doping vacancy and applying strain, Appl. Phys. Lett. **104**, 132403 (2014).

[49] S. Wang, G.-D. Lee, S. Lee, E. Yoon, and J. H. Warner, Detailed atomic reconstruction of extended line defects in monolayer MoS_2, ACS Nano **10**, 5419 (2016).

[50] J. B. Goodenough, Spin-orbit-coupling effects in transition-metal compounds, Phys. Rev. **171**, 466 (1968).

[51] T. Zheng, Y.-C. Lin, Y. Yu, P. Valencia-Acuna, A. A. Puretzky, R. Torsi, C. Liu, I. N. Ivanov, G. Duscher, D. B. Geohegan *et al.*, Excitonic dynamics in Janus MoSSe and WSSe monolayers, Nano Lett. **21**, 931 (2021).

DOI: 10.1103/PhysRevB.106.235414
URN: urn:nbn:de:hbz:465-20230905-105729-7

Mehdipour, H., & Kratzer, P. (2022). Structural defects in a Janus MoSSe monolayer: A density functional theory study. *Physical Review B*, **106**, 235414. https://doi.org/10.1103/PhysRevB.106.235414